Wear 406–407 (2018) 166–172

Contents lists available at ScienceDirect

Wear

journal homepage: www.elsevier.com/locate/wear

Anti-erosive mechanism of a grooved surface against impact of particle-laden flow

Sohyun Jung, Eunjin Yang, Wonjong Jung, Ho-Young Kim*

Department of Mechanical and Aerospace Engineering, Seoul National University, Seoul 08826, Republic of Korea

ARTICLE INFO

Keywords:
Impact wear
Solid particle erosion
Erosion testing
Surface topography
Bio-tribology

ABSTRACT

Erosion is a mechanical process that determines the lifetime of many machine components, as well as the quality of the protective skins of some animals and plants. Here, we assess quantitatively the role of grooves on ductile erosive surfaces in reducing erosion caused by the impact of particle-laden flow. In particular, we focus on V-shape grooves that are much larger than the particles. The grooves can induce diversification of impingement angles, multiple impacts of a single particle, and air swirls. By measuring the erosion rates of smooth and grooved surfaces at different impingement angles, and imaging the particle motion with a high-speed camera, we show that the diversified impingement angle on the grooves plays a key role in reducing erosion. Further, we predict theoretically the optimal groove angle for maximal erosion reduction at different values of impact angle. Our findings provide a framework for the design of artificial anti-erosive surfaces and advance our understanding of the design principles that enable biological skins to display anti-erosive properties when subjected to particle-laden fluid streams.

1. Introduction

The lifetimes of many machinery components and construction materials are influenced significantly by their capacity to resist erosion and corrosion. Corrosion, a chemical/electrochemical reaction that destroys the material, is enhanced by the erosion of the material surface [1]. Therefore, understanding and controlling erosion play important roles in many industries [2–4]. Furthermore, erosion is responsible for shaping the earth through processes such as rainfall, river streams, sea waves, glacial motions, and landslides [5]. Among many physical causes contributing to the erosion of industrial and natural objects, here we are interested in the erosion caused by the impact of fluid flows laden with solid particles, e.g., slurry flows and dusty winds. Industrial examples that suffer from erosion mediated by the impact of particle-laden flows include slurry and powder transfer pipelines, the blades of wind power generators and turbomachinery, and outer panels of vehicles.

Previous research has shown that the impact of particles can cut, plastically deform, or fracture material's surface [6]. The factors affecting the rate of impact-induced erosion have been identified as the impingement angles [7–12], the impact velocity of the solid particles [9–15], the substrate properties [9,10,16], total mass of impacted particles [9,11,12,16], particle size [10,11,17–19], and particle shape [12,19,20]. A number of technologies have been developed to reduce such erosion, including a filter system [21,22], anti-erosion materials [23,24], and surface treatments such as chemical coating [25–27], laser treatment [28–30], and patterning [31–34].

Recently, there has been a growing interest in the anti-erosion mechanism of living creatures inhabiting harsh environments. Several creatures that live in the desert, e.g., a snake [35], sand fish [36], and scorpion [37], possess certain textures on their surface, which are known to effectively resist abrasive erosion. In addition, tamarisk trees that are found in dry environments with frequent sandstorms, are known to have corrugated barks that are resistant to erosion caused by the impact of sand particles [38]. Although the biologically-inspired surface texturing to reduce erosion is highly attractive for practical applications, the fundamental mechanism that underlies such anti-erosive performance currently remain elusive.

Numerical computations of flow fields around various groove patterns and consequent flow-induced erosion rates suggested that swirling airflow inside the grooves acts as an air cushion to weaken the impact of solid particles [31,32]. However, the proposed mechanism has not been supported by experimental measurements to date. In addition, other plausible functions of grooves such as their capacity to change particle impingement angle and the effect of multiple particle impacts upon reflection have not been investigated. Therefore, in the present work, we measured experimentally the erosion rates of smooth and grooved surfaces to quantify the anti-erosive characteristics of the

---

* Corresponding author.
E-mail address: hyk@snu.ac.kr (H.-Y. Kim).

https://doi.org/10.1016/j.wear.2018.04.008
Received 11 September 2017; Received in revised form 11 April 2018; Accepted 11 April 2018

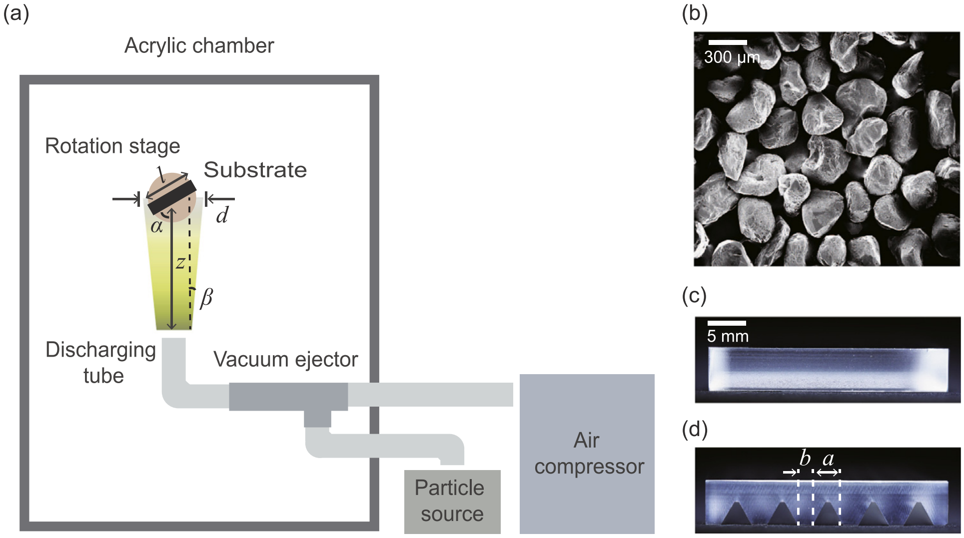

Fig. 1. (a) A schematic diagram of the experimental apparatus used to measure the erosion rates caused by particle-laden flow. The distance from the discharge tube and the center of the substrate is denoted as z, and d is the actual diameter of the particle stream. The side length of the square substrate is marked as l. α and β represent the impingement angle and the finite degree of particle dispersion, respectively. (b) SEM (scanning electron microscopy) image of quartz sand particles. (c) Side view of the smooth substrate. (d) Side view of the grooved surface with five equilateral triangular trenches.

patterned surfaces. The results of the measurements allowed us to identify the dominant mechanism of anti-erosive activity of the grooved surfaces over a finite range of impingement angles.

2. Materials and methods

The experimental apparatus used to generate particle-laden flows and to measure the erosion rates of substrates is schematically shown in Fig. 1(a). In a transparent acrylic chamber, a tube ejects high-speed airflow carrying particles onto a substrate at an impingement angle α, controlled by a rotation stage from 10° to 90°. The particle discharging tube is connected to a vacuum ejector that draws particles and air from a particle container and an air compressor, respectively. For the particles, we used white quartz sand (Sigma Aldrich), as shown in Fig. 1(b), whose average diameter and density are 230 μm and 2530 kg m^{-3}, respectively. The average diameter of the particles is defined as the diameter of a circle that has the same average area as the cross-sectional image of the grains. During the experiments, compressed air was injected into the vacuum ejector at a flow rate of 60 L min^{-1}, which drew the particles at a rate of 2.83 g s^{-1} and mixed them with the air. The particles were expelled through the discharging tube (6.5 mm inner diameter) at an exit velocity of 19 m s^{-1} as measured by a high-speed camera (Photron SA 1.1). The superficial velocity of air, U, was $U = 30$ m s^{-1} as measured by an air velocity meter (TSI VelociCalc 8346). We note that the wind speed in nature is typically below 20 m s^{-1} [39], which corresponds to a typical driving speed of automobiles.

As the substrate, we used an acrylic plate with a tensile strength and Young's modulus of 71.3 MPa and 3.2 GPa, respectively. We used two different types of surface morphology—smooth surfaces and V-shape grooved surfaces reported to be more anti-erosive than many of differently shaped grooves including U-, square-, and dome-shapes. [32]. For the smooth surface, we used a pristine surface with a roughness (defined as the ratio of the actual area to the projected area) of 1.0095 (± 0.0052) as measured by atomic force microscopy (Park Systems XE-70). The grooved surface possesses equilateral triangular trenches as carved by a tapping center. The apex of each triangle is rather blunt because of the limitation in the machining process. We ignored the effect of this bluntness on the results of our analysis since it represents only a very small portion of the entire groove size, and represents a spot where particle impacts is infrequent as a result of the shadowing by adjacent grooves. The triangles have a side of $a = 4$ mm long, and are spaced by $b = 2$ mm. The cross-sectional images of the substrates are shown in Fig. 1(c) and (d). The side length of the square substrate $l = 32$ mm. The distance from the discharge tube to the center of the substrate (z in Fig. 1(a)) is 14 cm.

Each erosion test lasted for one hour, after which we measured the mass loss W of a substrate by comparing its mass to that determined before the run. We repeated each test under the same conditions three times and calculated the average values. In addition, to visualize the particle paths near the substrates and to measure the coefficient of restitution upon impact, we used the high-speed camera running at 3×10^4 frames per second.

3. Results of erosion test

The results of the erosion tests are presented as a function of the impingement angle for both the smooth and the grooved surfaces. The erosion rate is defined as $\Pi = W/M$, which measures the mass loss of a substrate, W, due to the total mass of the impact particle, M. We note that the amount of particles encountering the substrate varies for different substrate orientations. For instance, only fractions of particles emitted from the tube impact onto the substrate with a low impingement angle α. Thus, M is calculated as $M = (L/d)M'$, from the known quantity, M', which represents the total mass of the ejected particles. Here, the projected length of the substrate $L = l \sin \alpha$, and the diameter of the particle stream near the substrate $d \approx 34$ mm, as illustrated in Fig. 1(a).

Fig. 2 shows the experimentally measured erosion rates of both smooth and grooved surfaces at different impingement angles. For the smooth surface, the erosion rate increased for small α until it reached a maximum at $\alpha = 20°$, and then monotonically decreased. The maximum erosion rate at $\alpha = 20°$ is 3.4 times higher than the minimum value determined at $\alpha = 90°$. For the grooved surface, the change in the erosion rate with α was relatively mild, and the rate reached its maximum at 10° and minimum at 40°, with the maximum rate being 1.5 times higher than the minimum value. In the following, we first explain the high sensitivity of the smooth surface to α. We then rationalize the erosion rates measured for the grooved surface using the quantitative erosion data for the smooth surface, in order to elucidate the dominant anti-erosive mechanism of the grooves. Finally, we describe a theoretical model to predict the optimal groove angles depending on the impact direction, and provide a rationale for the grooved surface of

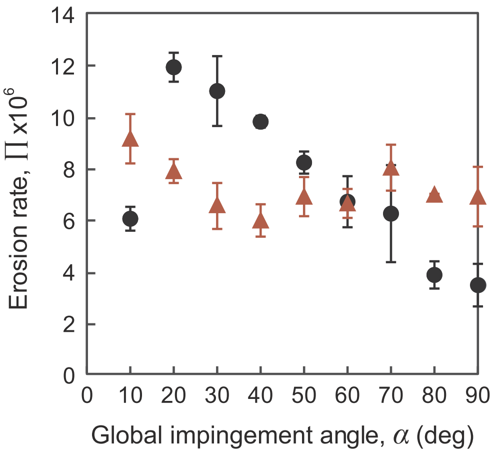

Impingement angle (°)	Thickness removed (μm)	
	Smooth	Grooved
10	7.1	22.2
20	25.9	26.2
30	34.5	29.0
40	36.2	27.6
50	34.7	35.7
60	40.7	41.3
70	40.0	36.7
80	25.9	30.4
90	23.5	29.7

Fig. 2. Experimental erosion rates determined for the smooth (black circles) and grooved surfaces (red triangles) as a function of the global impingement angle. Each error bar corresponds to a standard deviation obtained from three measurements. The table shows the experimental data of the thickness of material removed from the surfaces for one hour.

tamarisk trees.

It is known that the physical mechanism leading to erosion induced by particle impact varies with the impingement angle, α [6,40]. For low value of α, the cutting of the surface is mainly responsible for erosion as illustrated in Fig. 3(a). However, as α increases, the dominant mechanism changes to plastic deformation and brittle fracture, as shown in Fig. 3(b-c), as α increases. The SEM (scanning electron microscopy) images of the surfaces of the smooth substrate after the erosion test at different values of α are shown in Fig. 3(d–i). The images reveal apparent elongated cuts at low α (10–30°), and plastically deformed residue and fragments caused by fracture for high values of α (60° and 90°).

The experimental data collected for the smooth surfaces (Fig. 2) indicate a strong erosive capability of cutting and the weakest contribution of plastic deformation and fracture to erosion [9,40]. We speculate that the low erosion rate observed for the smooth surface at very low impingement angle α of 10° stems from the fact that the particles tend to slide along the surface without exerting significant normal force.

We compared the erosion rates measured for the smooth and grooved surfaces. Fig. 2 shows that the grooved surface exhibited a lower erosion rate than the smooth surface for α ranging from 20° to 60°. The relative decrease in the erosion rate, $(\Pi_s - \Pi_g)/\Pi_s$, where the subscripts s and g denote the smooth and grooved surface, respectively, reached a maximum of 40% at 30°. However, the erosion rate of the grooved surface was higher than that for the smooth surface when $\alpha > 60°$. Π_g is almost twice as high as Π_s at 90°.

4. Discussion

The behaviors of particles impacting on the grooved surfaces differed from those on the smooth surfaces in several aspects. Firstly, three different local impingement angles can be defined for the grooved surface as shown in Fig. 4(b), with only θ_1 being equal to the global impingement angle α. Secondly, a particle can collide with the grooved surface multiple times depending on α and the location of impact on the groove. Thirdly, the swirling airflow inside a groove can alter or weaken the velocity of a particle by acting as an air cushion. We investigated quantitatively the effects of these three mechanistic differences characteristic for grooved surfaces in order to identify the dominant factor leading to the anti-erosive performance of grooved surfaces over a finite range of α. Here, we neglect the mutual interaction of particles because of a very low fraction of particles volume(V_p) in air (V_a), $V_p/(V_a + V_p) = 1.8 \times 10^{-3}$ [41].

Prior to the quantitative estimation, it should be noted that we made the following modeling assumptions for the erosion process. Specifically, the particle direction is assumed to be perpendicular to the plane of $\alpha = 90°$ before impact. Also, the distribution and velocity of the particles are assumed to be uniform regardless of their position. These assumptions are based on the previous works showing that particle-laden jet flow with a high Stokes number ($St > 50$) exhibits small dispersion and relatively uniform distribution and velocity of particles [42–44]. Here, St is defined as the ratio of the response time of a particle to the characteristic time scale of the fluid, and it is ~ 100 for the flow between the discharging tube and the substrate with the characteristic length of z in Fig. 1. The detailed definition of St appears in §IV.C. In the actual experiments, a finite degree of particle dispersion is observed, but the dispersion angle, denoted as β in Fig. 1(a), is as low as 5.6°, thus allowing us to assume a nearly straight particle path.

4.1. Diversification of impingement angle

Fig. 4(b) illustrates the local impingement angle of each groove side, such that $\theta_1 = \alpha$, $\theta_2 = 120° - \alpha$, and $\theta_3 = \alpha - 60°$. As seen in the data obtained for the smooth surfaces (Fig. 2), the erosion rate is sensitive to the impingement angle of the particles. Since each side of the groove contributes to the total erosion, one may write the total mass loss as:

$$W = \sum_{i=1}^{3} w_i, \tag{1}$$

where w_i is the mass loss of the surfaces at an impingement angle θ_i in the grooved surface. We have $w_i = \pi_i m_i$, where π_i and m_i represent the erosion rate and impact particle mass of the grooved surface at impingement angle θ_i, respectively. The definition of the erosion rate leads us to write the erosion rates of the grooved surfaces, Π', as follows:

$$\Pi' = \frac{\sum_{i=1}^{3} w_i/s_i}{M/S}, \tag{2}$$

where S is the total surface area of the grooved substrate subject to erosion. In addition, $s_1 = n_s b$, $s_2 = n_g a$ for $\alpha \geq 60°$ and $s_2 = \frac{1}{2}[n_g a\{1 + \sqrt{3}\tan(\alpha - 30°)\}]$ for $\alpha < 60°$, and $s_3 = n_g a$ for $\alpha > 60°$ and $s_3 = 0$ for $\alpha \leq 60°$, where n_s and n_g are the number of spaces and grooves, respectively, and a and b are the lengths indicated in Fig. 4(b). The surface area of the grooved substrate subject to erosion is calculated considering the shadow effect, i.e. particles that cannot hit a part of each groove directly when $\alpha < 90°$.

Now we assume that the erosion rate of each surface π_i is identical to the value measured for the smooth surface in Fig. 2. This assumption would be valid provided that the particle trajectories and velocities were unaffected by the grooves. We examine such effects in the

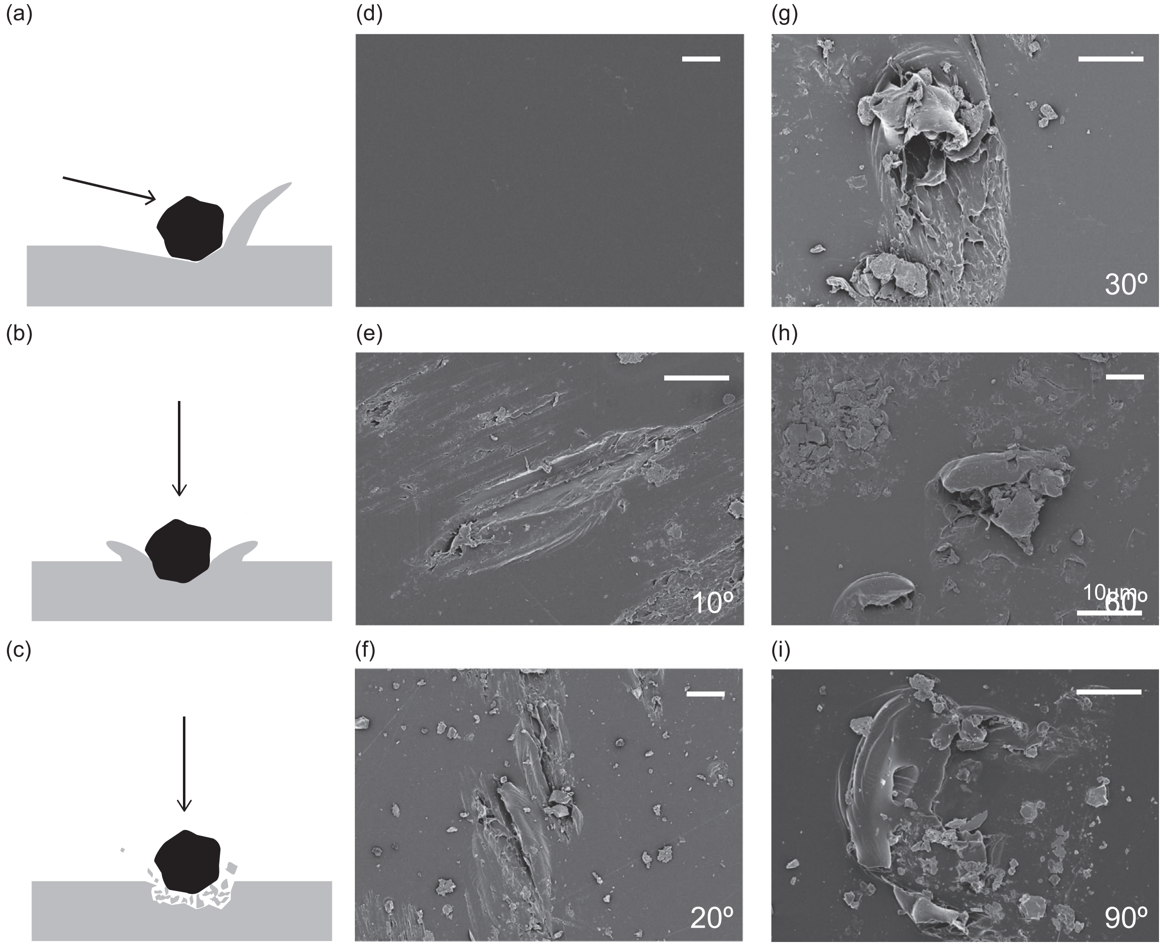

Fig. 3. Cartoon representation of different erosion mechanisms: (a) cutting; (b) plastic deformation; (c) brittle fracture. SEM images of surfaces: (d) smooth surface before the erosion test; (e–i) the smooth surfaces bombarded for 15 s with particle-laden flow at different impingement angles α (denoted in each image). Scale bars, 10 μm.

following sections, and here proceed with the proposed assumption. We substitute the values of erosion rates measured for the smooth surfaces for π_i in Eq. (2) to obtain the total erosion rate of the grooved surface Π'. We compare the estimated erosion rates with the experimentally measured values for different values of α in Fig. 4(c). Our estimation reproduces the trend in the experimental data fairly well. The relative error between the experimental(Π'_x) and estimated data(Π'_s), $\eta = |\Pi'_s - \Pi'_x|/\Pi'_x$, is on average 9%, with the exception of $\alpha = 10°$, at which point it reaches 24%. Therefore, the diversification of the impingement angle is considered to be the dominant mechanism of anti-erosive activity of the grooved surface, provided that the effects arising from other factors, which are discussed below in more detail, are insignificant.

4.2. Multiple impacts

When a particle enters a groove, it can hit the surface multiple times, as shown in Fig. 5(c–d), or it can hit it only once, as shown in Fig. 5(a–b), depending on the value of α and the impact location. We assumed the regular reflection, i.e., we assumed that the angles of incidence and reflection are identical, because of the low roughness of eroded surfaces. Our measurements revealed that the mean depth and cycle of roughness after 1-h long erosion test at $\alpha = 20°$, where the erosion is the severest, are 399 ± 186 nm and 5 ± 1.3 μm, respectively. The deviation in the reflection angle under such surface conditions was calculated to be only 2.3° using the particle-wall contact model [45].

A geometric consideration based on the assumption of regular reflection reveals that a particle can hit the surface up to three times in our grooves at $\alpha > 60°$, twice for $30° < \alpha \leq 60°$, and once for $\alpha \leq 30°$. The number of impacts also depends on the impact location as illustrated in Fig. 5(e). The surface area where multiple impacts are possible, S', is $\sqrt{3}\,n_g a \tan(\alpha - 30°)$ for $30° < \alpha < 60°$ and $S - s_1$ for $\alpha \geq 60°$.

The velocity and momentum of a particle decrease when it hits the substrate. In order to include this effect in the evaluation of erosion rates that are caused by multiple impacts, we measured the coefficient of restitution (ϵ), i.e., the ratio of velocity after impact to that before the impact. For the quartz sand grains impacting on the acrylic surface with the velocity 19 $\mathrm{m\,s^{-1}}$, as used in our erosion test, ϵ was measured to be 0.49 (± 0.07) over 50 runs. For erosion caused by the impact of solid particles, the mass loss W is known to be scaled as $W \sim V^x$ where V is the impact velocity and x depends on the properties of the substrate [11,13,14]. For brittle polymer substrates, x ranges from 3 to 5 [13,14].

The additional mass loss caused by the second and third impact of particles is respectively expressed as $\epsilon^x \Pi_\gamma MS'/S$ and $\epsilon^{2x} \Pi_\delta MS'/S$, where γ and δ are the local impingement angles of the particles during the second and third impact, respectively. Based on the estimated erosion rate, we included the effects of multiple impacts and plotted the results in Fig. 5(f). Here, we used $x = 3$ and $x = 5$ to determine the upper and lower bounds of the erosion rates, respectively, and assumed that the particles impact as many times as possible.

It is immediately apparent that the effect of multiple impacts is insignificant—the erosion rate is increased compared to the single-impact only erosion rate at most by 7% (at 60°). It can be attributed to the fact that the erosion rate decreases dramatically after the first impact,

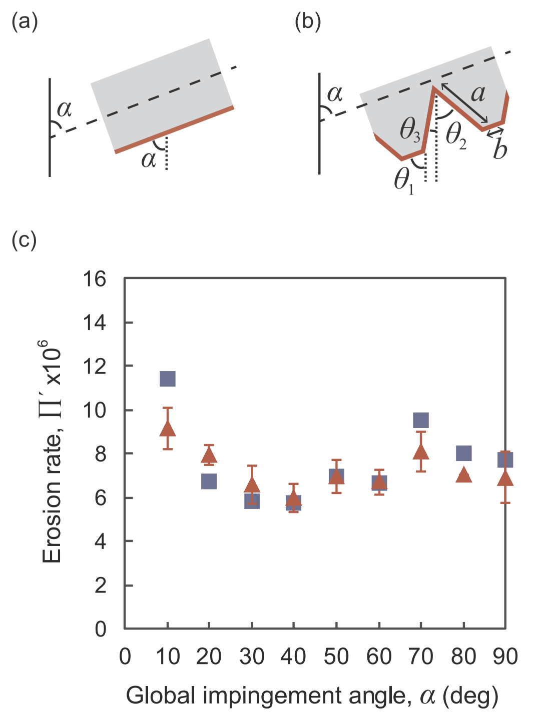

Fig. 4. Illustrations showing the local impingement angles on (a) a smooth surface and (b) a grooved surface. θ_1, θ_2, and θ_3 denote local impingement angles of faces 1, 2, and 3, respectively. (c) Comparison of the experimental (red triangles) and estimated (blue squares) erosion rates of the grooved surface as a function of α. Each error bar corresponds to a standard deviation obtained from three measurements. The estimated values were calculated using Eq. (2).

as well as the fact that only relatively small area allows for multiple impacts after the first collision. Although the decrease in the erosion rate after the first impact depends greatly on x and ϵ, metal substrates, as well as the acrylic substrate used in this study, are expected to be largely unaffected by multiple impacts for the following reason. The coefficients of restitution (ϵ) of sand particles on metals, such as 2024 aluminum, 6A1-4V titanium, AM 355, and RENE 41, are reported to be below 0.5 at impingement angles over 15° [46]. This coefficient ranges from 0.3 to 0.4 at impingement angles in the range of 60–90°, where the multiple impacts are the most likely to occur. The value of ϵ decreases with increasing particle impact velocity [47]. For ductile metals such as aluminum, titanium and copper, the exponent x ranges from 2 to 3. Owing to the low ϵ, the effect of multiple impacts is thus predicted to be negligible for metal substrates.

4.3. Swirls inside grooves

When a fluid flows over the grooves, internal recirculation is generated inside the cavity, whose characteristic flow speed is much smaller than that of the external flow [31,48,49]. It was previously suggested that as particle-laden flows approach a grooved surface, the swirls inside the groove reduce the impact velocities of the particles or deflect the particle trajectory to prevent particle collision [31,32]. We assess the effect of swirls occurring inside the grooves on the erosion rate in the following.

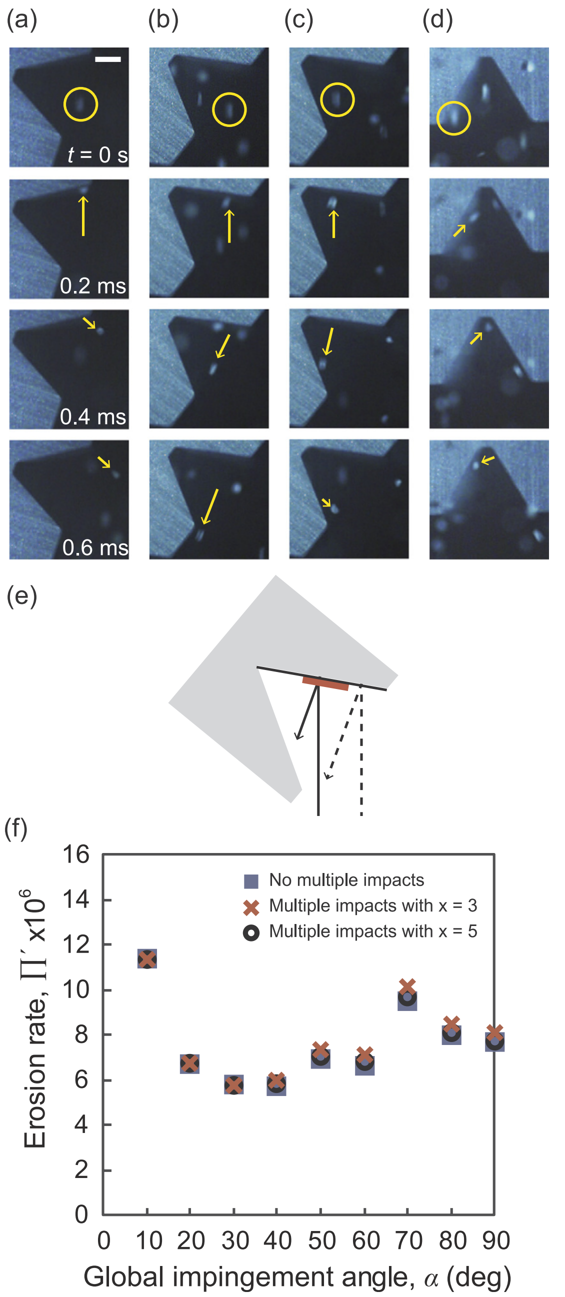

Fig. 5. Sequential images of particles impacting on grooved surface obtained at different values of the global impingement angle α: (a) $\alpha = 20°$; (b) $\alpha = 40°$, with impact occurring outside of the multiple impact zone; (c) $\alpha = 40°$, with impact occurring inside of the multiple impact zone; (d) $\alpha = 90°$, with impact occurring inside of the multiple impact zone. Scale bars = 1 mm. (e) Schematic representation of the multiple impact zone is shown in red. The solid (broken) line corresponds to the path of a particle experiencing multiple (single) impacts. (f) Comparison of the estimated erosion rates with multiple impacts ignored (blue squares) and considered (red crosses and black circles). The red crosses and black circles correspond to the estimated values obtained under the assumption that $x = 3$ and 5, respectively, in the mass loss - velocity model.

The Stokes number indicates whether the suspended particles will follow the fluid stream ($St \ll 1$) or not ($St \gg 1$). This number is defined as $St = (\rho_p d_p^2 \Delta u)/(18 \mu a)$, where ρ_p and d_p are respectively the density and the diameter of the particle, and μ is the dynamic viscosity of the fluid. The characteristic length a is the width of the mixing layer where the flow pattern changes the entrance of a groove in our case. Δu indicates the velocity difference between the two streams with different flow patterns. Under the present experimental conditions, where $\Delta u \sim 10\ \mathrm{m\,s^{-1}}$, we obtain $St \sim 10^3$, which suggests that the particle velocity is hardly affected by the swirls. Because Δu tends to increase with the flow velocity, particles impacting with a velocity higher than currently tested will still be unaffected by the swirling flow [50].

We can further confirm the insignificant effect of swirls by comparing the kinetic energy density of the particles (E_p) with the rotational kinetic energy density of the swirls (E_s). We write E_p as $E_p \sim \rho_p U^2$

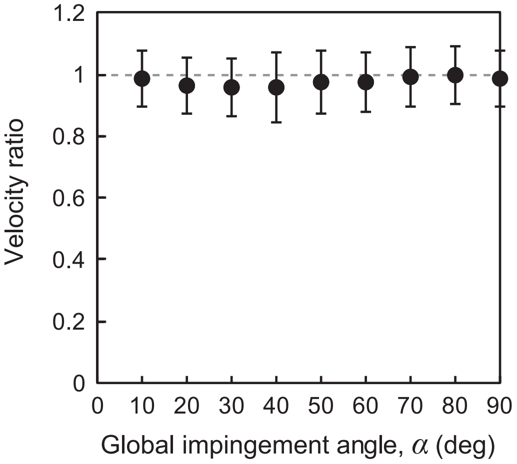

Fig. 6. The ratio of particle velocity inside the groove relative to the velocity of the particles approaching the groove. Fifty measurements were made for each global impingement angle. The error bar corresponds to the standard deviation.

and $E_s \sim \rho_a r^2\omega^2$, where ρ_a is the density of air, $r \sim 10^{-3}$ m is the radius of a swirl, and ω is the angular velocity of a swirl. Here, we estimate $\omega \sim v_s/r$ with v_s being the tangential velocity of the swirl in the order of $1\ \mathrm{m\,s^{-1}}$ [31,49]. The energy ratio $E_s/E_p \sim 10^{-5}$, so that E_p dominates over E_s.

The negligible impact of air swirls on the particle movement is therefore confirmed not only by the negligible deflection of the particle path (see Fig. 5(a–d)) but also by our experiments where the particle velocity was measured using a high-speed camera. Fig. 6 shows the ratio of the particle velocity inside the groove to the velocity of the particle approaching the groove ($19\ \mathrm{m\,s^{-1}}$). This figure reveals that the ratio is nearly at unity, with a minimum of 0.96 at $\alpha = 30°$.

4.4. Theory for the optimal groove angle and tamarisk

Having identified the dominant role of the impingement angle diversification in the reduction of erosion, we elaborate our theory to predict the optimal angle of the groove triangles as a function of the global impingement angle. We calculate the erosion rates for the grooved surfaces consisting of isosceles triangles with various base angles ϕ, as illustrated in the inset of Fig. 7. Following the same procedure as adopted in §IV.A, we use the data collected for the erosion rates of the smooth surfaces and consider the modification of local impingement angles caused by the grooves. Fig. 7(a) displays the dependence of the erosion rate of various groove angles on the global impingement angle. We can see that all grooved surfaces exhibit erosion rates that are lower than the corresponding rates obtained for the smooth surfaces when α ranges from 20° to 50°. In addition, one can find at least one case where the grooved surface has a lower erosion rate than the smooth surface for α between 10° and 70°. Each global impingement angle α has an optimum groove angle that minimizes the erosion rate as shown in Fig. 7(b).

Our understanding of the role of grooves in the reduction of erosion allows us to rationalize the anti-erosive characteristics of botanical cylindrical surfaces with grooves such as those founded in the tamarisk. Wood, in general, mainly consists of four polymers of cellulose, hemicellulose, lignin, and pectin, which are eroded in ductile manner [51]. In addition, the mechanical properties of tamarisk such as Young's modulus (1.2 GPa) and ultimate strength (43.4 MPa) are similar to those of acrylic (3.2 GPa and 64.8 MPa, respectively) [38]. We can calculate the erosion rates of cylindrical acrylic surfaces with and without grooves along the same line as delineated above. For the cylinder with a radius of 400 mm, bearing equilateral triangular grooves of 4 mm in width, i.e., sizes that corresponding to a typical 50-year-old tamarisks [52,53], we find that the erosion rate of the grooved surface is smaller than or equal to that of the smooth surface over 73% of the total surface area of the half cylinder facing wind. Therefore, the grooved cylindrical trunk appears to be the Nature's efficient means of resisting erosion under dusty winds with no preferred direction.

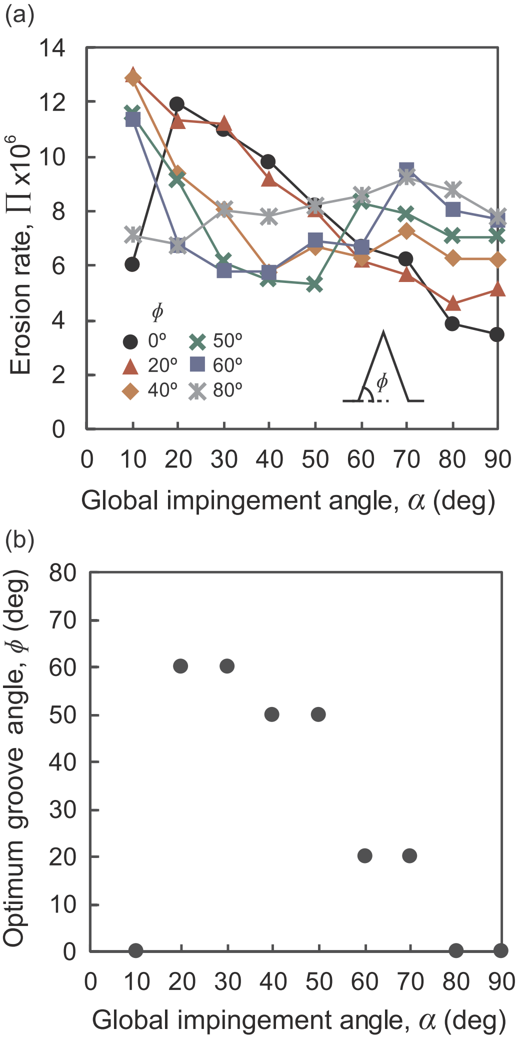

Fig. 7. (a) Comparison of the estimated erosion rates of triangular grooved surfaces with different base angles ϕ. The data for $\phi = 0$ corresponds to the experimental results obtained for the smooth surface. (b) The optimum base angle of isosceles triangular grooves as a function of the global impingement angle.

5. Conclusions

In the present work, we have evaluated quantitatively the erosion rates of smooth and V-shape grooved solid surfaces under the impact of particle-laden flows. The grooves on the surface were shown to reduce the erosion rate at impingement angles ranging from 20° to 60°, while the smooth surface was more resistant to erosion at impingement angles outside of this angle range. The anti-erosive range of global impingement angles of a grooved surface changes according to the ductility of the target surface. The range obtained in this work is valid for the surfaces eroded in a ductile manner like polymers including acrylic plates [54]. Other studies have shown that the grooves on the surfaces eroded in brittle manner reduce the erosion rate at high impingement angles (e.g., 90°) [55,56].

The dependence of the grooved surface's erosion rate on the impingement angle was successfully explained by considering the diversification of the local impact angle caused by the presence of the grooves. By contrast, other factors, including the multiple impacts of particles and the air swirls within grooves, were shown to exert negligible effects on erosion. The absence of significant impact observed for both the multiple impact scenario and the air swirls is a natural consequence of high *Re* associated with the impact of particle-laden flows because the coefficient of restitution decreases rapidly with the impact velocity and the rotational velocity of the swirl is not high enough to influence the particle movement.

Our approach of inducing erosion rate of grooved surfaces based on the erosion rates measured for flat substrates with varying incident angles can be applied to differently shaped grooves as well. Our findings that the grooved surface can reduce erosion under certain global impingement angles suggests both the promise and limitation of this biologically inspired anti-erosive approach. When the ambient flow direction is either nearly parallel or perpendicular to the surface, which is eroded in ductile manner, the grooves aggravate erosion. However, one can benefit from the grooves if the direction of the surface can be tuned in such a way that the impingement angles lie in the range of effective anti-erosion (i.e., $20 - 60°$). Meanwhile, cylindrical surfaces with grooves are shown to be more resistant to erosion when compared to smooth surfaces, regardless of the wind direction—a phenomenon that is exploited and manifested in tamarisks.

Acknowledgement

This work was supported by the National Research Foundation of Korea (Grant Nos. 2016901290 and 2016913167) through SNU IAMD.

References

[1] S. Zhou, M.M. Stack, R.C. Newman, Characterization of synergistic effects between erosion and corrosion in an aqueous environment using electrochemical techniques, Corrosion 52 (1996) 934–946.

[2] A. Forder, M. Thew, D. Harrison, A numerical investigation of solid particle erosion experienced within oilfield control valves, Wear 109 (1998) 344–352.

[3] P.F. Batcho, J.C. Moller, C. Padova, M.G. Dunn, Interpretation of gas-turbine response due to dust ingestion, J. Eng. Gas Turb. Power 11 (1987) 111–122.

[4] G. Grant, W. Tabakoff, Erosion prediction in turbomachinery resulting from environmental solid particles, J. Aircr. 12 (1975) 471–478.

[5] R. Huggett, in: Fundamentals of Geomorphology; Gerrard, J., Ed.; Routledge: New York, 2007; Vol. 2, Chapter 1.

[6] G.W Stachowiak, A.W. Batchelor, in: Engineering Tribology; Butterworth-Heinemann: The Netherlands, Amsterdam, 1993; Vol. 1, Chapter 11.

[7] I. Finnie, G.R. Stevick, J.R. Ridgely, The influence of impingement angle on the erosion of ductile metals by angular abrasive particles, Wear 152 (1992) 91–98.

[8] Y.I. Oka, H. Ohnogi, T. Hosokawa, M. Matsumura, The impact angle dependence of erosion damage caused by solid particle impact, Wear 203–204 (1997) 573–579.

[9] I. Finnie, Erosion of surfaces by solid particles, Wear 3 (1960) 87–103.

[10] Y.I. Oka, K. Okamura, T. Yoshida, Practical estimation of erosion damage caused by solid particle impact: part 1: effects of impact parameters on a predictive equation, Wear 259 (2005) 95–101.

[11] G.P. Tilly, W. Sage, The interaction of particle and material behaviour in erosion processes, Wear 16 (1970) 447–465.

[12] J.H. Neilson, A. Gilchrist, Erosion by a stream of solid particles, Wear 11 (1968) 111–122.

[13] K.V. Pool, C.K.H. Dharan, I. Finnie, Erosive wear of composite materials, Wear 107 (1986) 1–12.

[14] M. Roy, B. Vishwanathan, G. Sundararajan, The solid particle erosion of polymer matrix composites, Wear 171 (1994) 149–161.

[15] N. Miyazaki, N. Takeda, Solid particle erosion of fiber reinforced plastics, J. Compos. Mater. 27 (1993) 21–31.

[16] Y.I. Oka, M. Matsumura, T. Kawabata, Relationship between surface hardness and erosion damage caused by solid particle impact, Wear 162 (1993) 688–695.

[17] A. Misra, I. Finnie, On the size effect in abrasive and erosive wear, Wear 65 (1981) 359–373.

[18] E. Rabinowicz, A. Mutis, Effect of abrasive particle size on wear, Wear 8 (1965) 381–390.

[19] S. Bahadur, R. Badruddin, Erodent particle characterization and the effect of particle size and shape on erosion, Wear 55 (1979) 163–190.

[20] G.R. Desale, B.K. Gandhi, S.C. Jain, Effect of erodent properties on erosion wear of ductile type materials, Wear 261 (2006) 914–921.

[21] A. Filippone, N. Bojdo, Turboshaft engine air particle separation, Prog. Aerosp. Sci. 46 (2010) 224–245.

[22] N. Bojdo, A. Filippone, Comparative study of helicopter engine particle separators, J. Aircr. 51 (2014) 1030–1042.

[23] D.Y. Li, A new type of wear-resistant material: pseudo-elastic TiNi alloy, Wear 221 (1998) 116–123.

[24] R.H. Van der Jagt, B.H. Kolster, M.W.H. Gillham, Anti-wear/corrosion treatment of finished austenitic stainless steel components: the Hardcor process, Mater. Des. 12 (1991) 41–46.

[25] B.S. Mann, High-energy particle impact wear resistance of hard coatings and their application in hydroturbines, Wear 237 (2000) 140–146.

[26] B.S. Mann, V. Arya, HVOF coating and surface treatment for enhancing droplet erosion resistance of steam turbine blades, Wear 254 (2003) 652–667.

[27] D.S. Rickerby, P.J. Burnett, The wear and erosion resistance of hard PVD coatings, Surf. Coat. Technol. 33 (1987) 191–211.

[28] P.H. Chong, H.C. Man, T.M. Yue, Microstructure and wear properties of laser surface-cladded Mo-WC MMC on AA6061 aluminum alloy, Surf. Coat. Technol. 145 (2001) 51–59.

[29] D. Triantafyllidis, L. Li, F.H. Stott, Surface treatment of alumina-based ceramics using combined laser sources, Appl. Surf. 186 (2002) 140–144.

[30] K.F. Alabeedi, J.H. Abboud, K.Y. Benyounis, Microstructure and erosion resistance enhancement of nodular cast iron by laser melting, Wear 266 (2009) 925–933.

[31] Z. Han, Z. Junqiu, G. Chao, W. Li, L. Ren, Erosion resistance of bionic functional surfaces inspired from desert scorpions, Langmuir 28 (2012) 2914–2921.

[32] Z. Han, W. Yin, J. Zhang, J. Jiang, S. Niu, L. Ren, Erosion-resistant surfaces inspired by tamarisk, J. Bionic Eng. 10 (2013) 479–487.

[33] W. Yin, Z.W. Han, H.L. Feng, J.Q. Zhang, H.N. Cao, Y. Tian, Gas-solid erosive wear of biomimetic pattern surface inspired from plant, Tribol. Trans. 60 (2017) 159–165.

[34] G. Chen, D.L. Schott, G. Lodewijks, Bionic design methodology for wear reduction of bulk solids handling equipment, Part. Sci. Technol. 35 (2016) 525–532.

[35] H.A. Abdel-Aal, M.E. Mansori, S. Mezghani, Multi-scale investigation of surface topography of ball python (Python regius) shed skin in comparison to human skin, Tribol. Lett. 37 (2010) 517–527.

[36] W. Baumgartner, F. Saxe, A. Weth, D. Hajas, D. Sigumonrong, J. Emmerlich, M. Singheiser, W. Böhme, J.M. Schneider, The sandfish's skin: morphology, chemistry and reconstruction, J. Bionic Eng. 4 (2007) 1–9.

[37] V. Fet, G.A. Polis, W.D. Sissom, Life in sandy deserts: the scorpion model, J. Arid Environ. 39 (1998) 609–622.

[38] Z. Han, W. Yin, J. Zhang, S. Niu, L. Ren, Active anti-erosion protection strategy in tamarisk (Tamarix aphylla), Sci. Rep. 3 (2013) 3429.

[39] R. Wanninkhof, Relationship between wind speed and gas exchange over the ocean, J. Geophys. Res. 97 (1992) 7373–7382.

[40] I. Finnie, Some reflections on the past and future of erosion, Wear 186–187 (1995) 1–10.

[41] S. Elghobashi, On predicting particle-laden turbulent flows, Appl. Sci. Res. 52 (1994) 309–329.

[42] H. Zhou, G. Mo, K. Cen, Numerical investigation of a gas-solid turbulent jet flow with Reynolds number of 4500 using lattice Boltzmann method, Appl. Math. Model. 40 (2016) 565–577.

[43] K. Luo, J. Fan, K. Cen, Modulations on turbulent characteristics by dispersed particles in gas-solid jets, Proc. R. Soc. Lond. 461 (2005) 3279–3295.

[44] S.E.T.W.M.A. Elghobashi, T. Abou-Arab, M. Rizk, A. Mostafa, Prediction of the particle-laden jet with a two-equation turbulence model, Int. J. Multiphase Flow 10 (1984) 697–710.

[45] M. Sommerfeld, Modelling of particle-wall collisions in confined gas-particle flows, Int. J. Multiphase Flow 18 (1992) 905–926.

[46] W. Tabakoff, A. Hamed, D.M. Murugan, Effect of target materials on the particle restitution characteristics for turbomachinery application, J. Propul. Power 12 (1996) 260–266.

[47] X. Zhang, L. Vu-Quoc, Modeling the dependence of the coefficient of restitution on the impact velocity in elasto-plastic collisions, Int. J. Impact Eng. 27 (2002) 317–341.

[48] S. Tantirige, A. Iribarne, M. Ojha, O. Trass, The turbulent boundary layer over single V-shaped grooves, Int. J. Heat Mass Transf. 37 (1994) 2261–2271.

[49] J.R. Koseff, R.L. Street, The lid-driven cavity flow: a synthesis of qualitative and quantitative observations, J. Fluids Eng. 106 (1984) 390–398.

[50] N. Zhuang, F.S. Alvi, M.B. Alkislar, C. Shih, Supersonic cavity flows and their control, AIAA J. 44 (2006) 2118–2128.

[51] L.J. Gibson, The hierarchical structure and mechanics of plant materials, J. R. Soc. Interface 9 (2012) 2749–2766.

[52] A.N. Sadegh, M. Kiaei, A.H.M.A.D. Samariha, Experimental characterization of shrinkage and density of Tamarix aphylla wood, Cell. Chem. Technol. 46 (2012) 369–373.

[53] B.L. Everitt, Ecology of saltcedar - A plea for research, Environ. Geol. 3 (1980) 77–84.

[54] H. Getu, J.K. Spelt, M. Papini, Conditions leading to the embedding of angular and spherical particles during the solid particle erosion of polymers, Wear 292 (2012) 159–168.

[55] P.J. Slikkerveer, Model for patterned erosion, Wear 233 (1999) 377–386.

[56] A. Ghobeity, T. Krajac, T. Burzynski, M. Papini, J.K. Spelt, Surface evolution models in abrasive jet micromachining, Wear 264 (2008) 185–198.